Journal Name

ARTICLE

Lithium manganese oxyfluoride as a new cathode material exhibiting oxygen redox

Received 00th January 20xx,
Accepted 00th January 20xx

DOI: 10.1039/x0xx00000x

www.rsc.org/

Robert House[a], Liyu Jin[a], Urmimala Maitra[a], Kazuki Tsuruta[b], James Somerville[a], Dominic Forstermann[a], Felix Massel[c], Laurent Duda[c], Matthew R. Roberts[a] and Peter G. Bruce[a]

The quantity of charge stored in transition metal oxide intercalation cathodes for Li or Na batteries is not limited by transition metal redox reactions but can also access redox reactions on O, examples include $Li_{1.2}Ni_{0.13}Mn_{0.54}Co_{0.13}O_2$, $Li_2Ru_{0.75}Sn_{0.25}O_3$, $Li_{1.2}Nb_{0.3}Mn_{0.4}O_2$, Na_2RuO_3 and $Na_{2/3}Mg_{0.28}Mn_{0.72}O_2$. Here we show that oxyfluorides can also exhibit charge storage by O-redox. We report the discovery of lithium manganese oxyfluoride, specifically the composition, $Li_{1.9}Mn_{0.95}O_{2.05}F_{0.95}$, with a high capacity to store charge of 280 mAh g^{-1} (corresponding to 960 Wh kg^{-1}) of which almost half, 130 mAh g^{-1}, arises from O-redox. This material has a disordered cubic Rocksalt structure and the voltage-composition curve is significantly more reversible compared with ordered Li-rich layered cathodes. Unlike lithium manganese oxides such as the ordered layered Rocksalt Li_2MnO_3, $Li_{1.9}Mn_{0.95}O_{2.05}F_{0.95}$ does not exhibit O loss from the lattice. The material is synthesised using a simple, one-pot mechanochemical procedure.

Introduction

Lithium-rich layered transition metal (Tm) oxides based on manganese, such as $Li_{1.2}Ni_{0.13}Mn_{0.54}Co_{0.13}O_2$ (NMC) and $Li_{1.2}Ni_{0.2}Mn_{0.6}O_2$, are being hotly pursued as future cathode materials in competition with the Ni-rich $Li[Ni_{0.8}Co_{0.15}Al_{0.05}]O_2$ (NCA) because of the potentially lower cost of the lithium rich materials[1–10]. Their high capacities, typically, 250 to 300 mAh g^{-1}, arise from storing charge utilising both transition metal and O-redox. Alkali metal rich 4d and 5d transition metal oxides have also been shown to exhibit O-redox[11–15]. These materials are all based on ordered structures.

Recently, there has been increasing interest in disordered intercalation compounds, especially disordered Rocksalt structures. It has been shown that provided the Li:Tm ratio is sufficiently large to permit enough low energy percolation pathways[16–18], then they can function as intercalation compounds and with relatively high capacities. Several examples of these Li-rich disordered intercalation compounds have been reported, including Li_3NbO_4-based systems[19–21], $Li_{1.2}Ti_{0.4}Mn_{0.4}O_2$[22] and $Li_{1.2}Ni_{1/3}Ti_{1/3}Mo_{2/15}O_2$[18]. Synthesis of these heavy metal and Li_2TiO_3-based disordered Rocksalts is possible by conventional high temperature methods. However, for Mn-rich 3d transition metal compounds, high temperature synthesis usually forms ordered phases such as Li_2MnO_3 or orthorhombic $LiMnO_2$. To counter this, high energy mechanochemical ball-milling methods have been used to synthesise all-manganese Rocksalts. The most recent compounds presented by Freire et al. using this method were of reported compositions Li_2MnO_3[23] and $Li_4Mn_2O_5$[24]. The latter displays high initial capacity of 355 mAh g^{-1} when charged at a low rate (6 mAg^{-1}) over a large voltage range (1.3V to 4.8V), but fades substantially in capacity over the following cycles.

Mechanochemical ball-milling has also been used as a means of incorporating fluoride anions into these structures to harness the element's high electronegativity in an effort to increase the voltage of these materials and further to reduce the valence of the transition metal by substituting O^{2-} for F^-. Composite structures comprising intimately mixed, but structurally distinct, phases of LiF and MO (where M = Mn, Fe, Co) have been studied and a surface conversion reaction mechanism proposed to explain their reactivity in Li-ion batteries[25,26]. Other researchers have managed to access solid solution oxyfluoride Rocksalt phases by using higher ball-milling energies. In pioneering work by Hahn and Kobayashi and their respective co-workers, lithiated oxyfluoride materials were synthesised based on V[27–29] and Ni[30,31]; two transition metals which undergo multiple valence state changes. However, these have involved prolonged reaction times of over 100 hrs and impurities introduced from abrasion of the milling jar medium.

Here we present for the first time an all-manganese lithium transition metal oxyfluoride, with a disordered Rocksalt structure which exhibits a large and reversible capacity to store charge utilising Tm and O-redox. This material exhibits a discharge capacity of ~280 mAh g^{-1} (corresponding to 960 Wh kg^{-1}) after the initial charge, makes it comparable to $Li_{1.2}Ni_{0.13}Mn_{0.54}Co_{0.13}O_2$ which shows ~270 mAh g^{-1} (~950 Wh kg^{-1})[6] and $Li_{1.2}Ni_{0.2}Mn_{0.6}O_2$ ~250 mAh g^{-1} (~880 Wh kg^{-1})[32] at the

[a] Departments of Materials and Chemistry, University of Oxford, Parks Road, Oxford OX1 3PH, UK.
[b] Japan Synchrotron Radiation Research Institute (JASRI), 1-1-1 Kouto, Sayo, Hyogo 679-5198, Japan
[c] Department of Physics and Astronomy, Division of Molecular and Condensed Matter Physics, Uppsala University, Box 516, S-751 20 Uppsala, Sweden
Electronic Supplementary Information (ESI) available: [details of any supplementary information available should be included here]. See DOI: 10.1039/x0xx00000x

same charging rate and in the same voltage range. The prepared lithium manganese oxyfluoride shows a reversible voltage-composition profile on the first cycle and no significant oxygen loss in contrast to the layered Li Rich materials. Using soft X-ray radiation we show that the oxygen anions are responsible for charge compensation in line with our previous findings in the layered Li-rich materials [6,7].

Results and Discussion

Material Characterisation

We targeted the composition Li_2MnO_2F and thus mixed LiF, Li_2O and Mn_2O_3 in a 2:1:1 molar ratio and sealed in zirconia jars in an argon-filled glovebox. The mixture was then ball-milled for 18 hours at 750rpm in a Fritsch Pulverisette 7 planetary ball mill (further details are contained in the Experimental section of the Supplementary Information). A Powder X-Ray Diffraction (PXRD) pattern of the pristine material was collected (Fig. 1) and fitted using the Reitveld method of refinement to the $Fm\bar{3}m$ cubic Rocksalt space group, full crystallographic data are outlined in Table S1.

Solid state ^{7}Li and ^{19}F magic angle spinning (MAS) NMR spectroscopy was carried out to study the local chemical environments of lithium and fluorine in the ball-milled material. As shown in Fig. 2, a substantial transformation is observed after ball-milling. The intense peak of LiF with chemical shift, δ = -204 ppm almost completely disappears suggesting near complete reaction. Meanwhile, as shown in the inset, a much broader peak (centred about δ = -174 ppm) emerges, which is

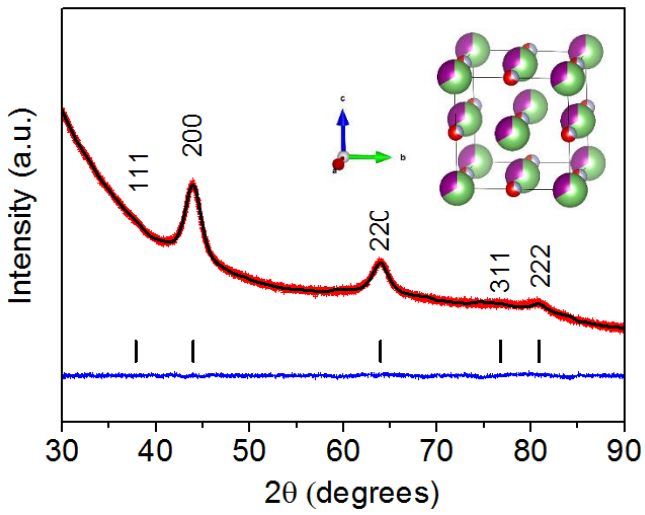

Fig. 1 Powder X-ray Diffraction pattern of pristine LMOF collected in a sealed glass capillary and refined using the Rietveld method to the $Fm\bar{3}m$ space group with cell parameter a = 4.1176(5) Å and χ^2 = 1.535. Site occupancies were fixed to the targeted composition and the cell parameter and peak width allowed to vary (Red curve = experimental diffraction pattern, black = calculated pattern, blue = difference plot and black tick marks = allowed reflections). Inset shows the cubic LMOF unit cell visualised using VESTA (red = oxygen, grey = fluorine, green = lithium and purple = manganese).

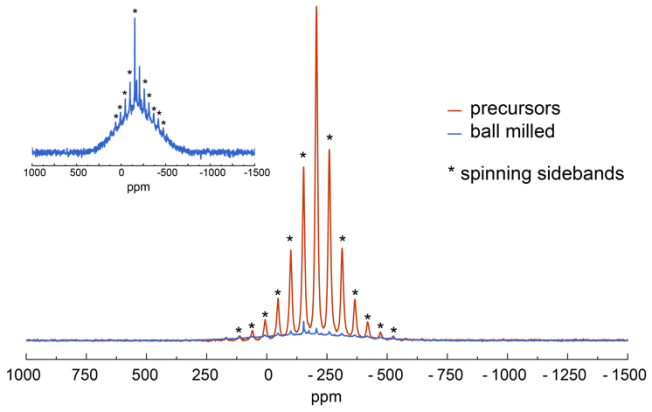

Fig. 2 ^{19}F solid state MAS NMR for a precursor mixture of LiF, Li_2O and Mn_2O_3 ground together in a mortar and pestle in a 2:1:1 ratio compared with that for the pristine LMOF. Spectra are normalised to account for sample mass. The inset gives a zoomed-in view of the spectrum of the ball-milled sample. The MAS rate was 20 kHz.

attributed to ^{19}F in the rock salt phase. This broad peak has Gaussian line shape with no resolved spinning sidebands suggesting it consists of many overlapped paramagnetic shifts[33] resulting from fluoride ions residing in a range of different local environments influenced by paramagnetic Mn in the immediate vicinity. This is consistent with a disordered phase[34]. Similar changes are observed in the ^{7}Li NMR spectrum which is sensitive to both Li_2O and LiF as described in Fig. S1.

Elemental composition analysis using ICP-OES confirmed the Li:Mn ratio as unchanged before and after milling at 2.03(3) and 1.99(3) respectively. Samples of the precursor mixture and the material after ball-milling were completely dissolved in concentrated HCl acid and liquid state ^{7}Li and ^{19}F NMR confirmed the Li:F ratio as unchanged before and after milling (Fig. S2). However, oxidation state analysis using iodometric titration indicated an average Mn oxidation state of around +3.3 demonstrating that, despite the ratios of Li:Mn:F being 2:1:1, the material is oxidised (Table S2). This degree of oxidation cannot be accounted for by post-synthesis reaction with air of Li_2MnO_2F to form $Li_{2-x}MnO_2F$ and Li_2O or Li_2CO_3 as there wasn't evidence of diamagnetic phase segregation from ^{7}Li NMR (Figure S1), nor can it be due to precursor impurities whose purity was verified. Therefore, we conclude that some oxidation must have occurred during synthesis resulting in a cation deficient phase with the true composition of $Li_{1.9}Mn_{0.95}[\ ]_{0.15}O_{2.05}F_{0.95}$, which we label LMOF.

The particle size and morphology of the ball-milled LMOF sample were assessed using a combination of Brunauer–Emmett–Teller (BET) surface area analysis and Scanning Electron Microscopy (SEM). The SEM images show a range of particle sizes typically from 0.1 to 0.5 microns (Fig. S3). The surface area from BET, 13.4(1) $m^2\ g^{-1}$, indicates an average particle size of 0.15 microns assuming spherical particles. These values are higher than the value extracted by Scherrer analysis of the wide peaks in the PXRD patterns, Fig. 1, of 5 nm. However, the peak broadening in PXRD relates to the coherence

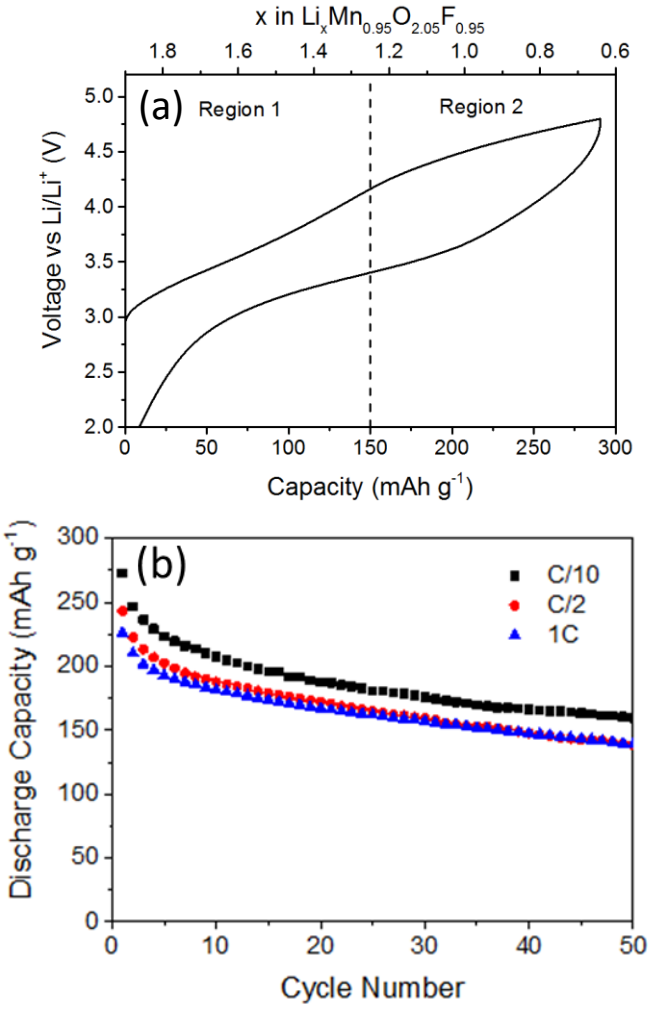

Fig. 3 (a) Charge-discharge curve for LMOF vs. lithium. First cycle is shown in the voltage range 2 V to 4.8 V at a rate of C/10 (22.4 mA g^{-1}). (b) Discharge capacity as a function of cycle number at progressively faster C-rates of C/10, C/2 and 1C.

length and hence size of ordered domains and not the particle size, which is larger as seen here.

Electrochemical Performance

Electrochemical charge/discharge profiles of LMOF are shown in Fig. 3. During the first charge to 4.8V a capacity of 291 mAh g^{-1} was observed. This can be segmented into regions 1 and 2 as shown in Fig 3a. The charge passed in region 1 is consistent with the theoretical capacity expected from the oxidation of $Mn^{3.3+}$ to Mn^{4+} (150 mAh g^{-1}, 0.65 $mol_{electrons}/mol_{LMOF}$). At the beginning of region 2 the gradient of the voltage profile changes and a further ~140 mAh g^{-1} (0.6 $mol_{electrons}/mol_{LMOF}$) of charge is extracted beyond the Mn^{4+} threshold, these two regions can be clearly resolved in the dQ/dV plot (Fig. S4). On subsequent discharge to 2V, 283 mAh g^{-1} of charge is recovered at an average potential of 3.4V (corresponding to an energy density of 960 Wh kg^{-1} at C/10 or 22.4 mA g^{-1}) beyond that which would be expected for complete reduction of Mn to +3 (~230 mAh g^{-1}).

To confirm that the lithium content varied as was anticipated from the charge passed in the electrochemical experiment, ICP-OES measurements were carried out on cathodes collected before cycling and at the end of charge and discharge (Table S3). Table S3 shows that the Li extracted and inserted varies in good accord with the total charge recorded indicating minimal contribution from electrolyte oxidation. To establish the scale of any oxidative decomposition process, operando mass spec. (Fig. S5) was employed. This shows that only trace amounts of CO_2 (a principle component evolved during the oxidation of carbonate electrolytes) were generated on charging (0.03 mol_{CO2}/mol_{LMOF} is observed compared to 1.30 $mol_{electrons}/mol_{LMOF}$ charge passed) thereby verifying only a negligible contribution to the charge compensation process from electrolyte oxidation. Beyond this explanation for additional capacity in excess of the $Mn^{3+/4+}$ redox couple, several studies have previously cited oxygen loss[6,7,35–37]. The OEMS experiment confirms that this was not the case here and leads us to anticipate that anionic redox processes are occurring within this material.

Spectroscopic Studies

To examine this further Mn L-edge and O K-edge soft X-ray absorption spectra (SXAS) were collected. The former, Fig. 4a, were collected using the inverse Partial Fluorescence Yield (iPFY) mode which is both bulk sensitive (to a probe depth of about 150 nm) and free of self-absorption effects[38]. The spectra show the expected change in the Mn $L_{2,3}$ peaks on charging to 4.8V as a result of Mn oxidation to +4. When fully charged the spectra appear consistent with the Mn^{4+} standard, MnO_2, indicating the absence of further Tm oxidation. On discharge the spectra return to a shape consistent with the original material with no evidence of the formation of Mn^{2+}. Therefore we can be certain that the Mn^{3+} to Mn^{4+} redox couple is the only redox active transition occurring on the manganese. If we consider the theoretical capacity of a completely active Mn^{3+} to Mn^{4+} redox couple then we would anticipate a theoretical capacity on both charge and discharge of ~230 mAh g^{-1}. Since the material clearly exceeds this then these results confirm the presence of an additional redox process during both the charge and discharge of LMOF.

The O K-edge data, Fig. 4b, collected on the same samples provide evidence that lattice oxygen plays a role in compensating this additional charge. The area under the pre-edge corresponding to the density of empty states in the hybridised O-2p/Mn-3d orbitals, increases on charging to 4.8V. This increase in intensity can be explained by the formation of hole states on O and Mn on charging. Evidence of a new feature appearing at 531.5 eV can also be seen on charging which is consistent with the changes we have seen previously for anion redox materials. On discharge the area of the O K-edge returns to close to that of the pristine material (with the evidence of some carbonate formation on discharge (534 eV)[39]). This conclusion is further reinforced by the Resonant Inelastic X-Ray

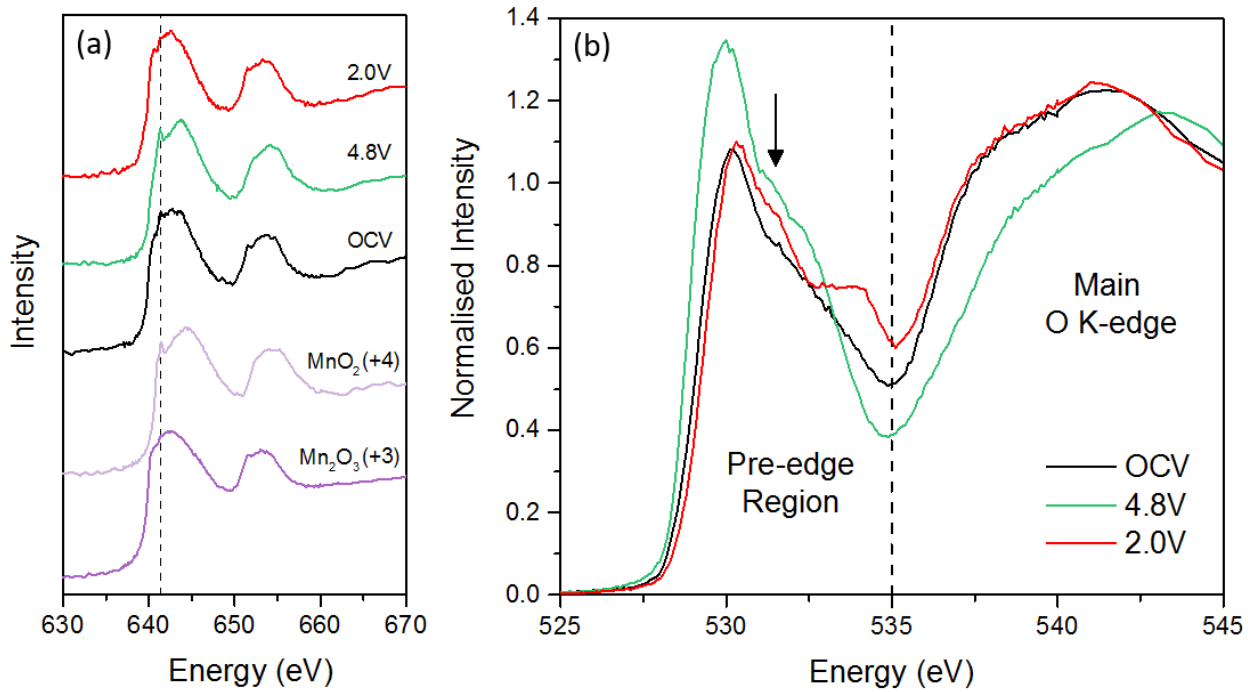

Fig. 4 (a) Mn L-edge XAS spectra collected in iPFY mode to probe Mn oxidation states. The $L_{2,3}$ peak energies change in line with oxidation of Mn to +4 on charge and then reduction back towards the oxidation state of the pristine on discharge. (b) O K-edge XAS spectra collected in bulk-sensitive PFY mode show an increase and decrease in intensity of the pre-edge region corresponding to the formation and filling of hole states in Mn-3d/O-2p hybridised orbitals. The arrow indicates the energy (531.5 eV) at which a new resonant feature appears. On discharge to 2V a feature at 534 eV appears which we attribute to CO_3^{2-} species formed at the interface between the electrode and electrolyte. Cathode samples were charged at a rate of C/10 (22.4 mA g^{-1}) and collected for *ex situ* measurement at OCV, end of charge (4.8V) and end of discharge (2V).

Scattering (RIXS) data in Fig. 5a which reveal a significant and reversible change on oxidation to 4.8V with two well resolved peaks between 522 and 528 eV as well as an elastic peak at 531.5 eV, very reminiscent of the RIXS spectra we observed for $Li[Li_{0.2}Ni_{0.13}Co_{0.13}Mn_{0.54}]O_2$ and $Li[Li_{0.2}Ni_{0.2}Mn_{0.6}]O_2$[6,7]. To further probe this new feature, RIXS mapping on the cathode charged to 4.8V was carried out, Fig 5b, and this indicates that these states are resonant in a narrow energy range (< 1 eV) and hence correspond to newly formed, localised electronic states on oxygen consistent with our previous findings for O-redox materials. To the best of our knowledge, this represents the first time that capacity from anion redox has been observed in this new class of oxyfluoride Rocksalt materials.

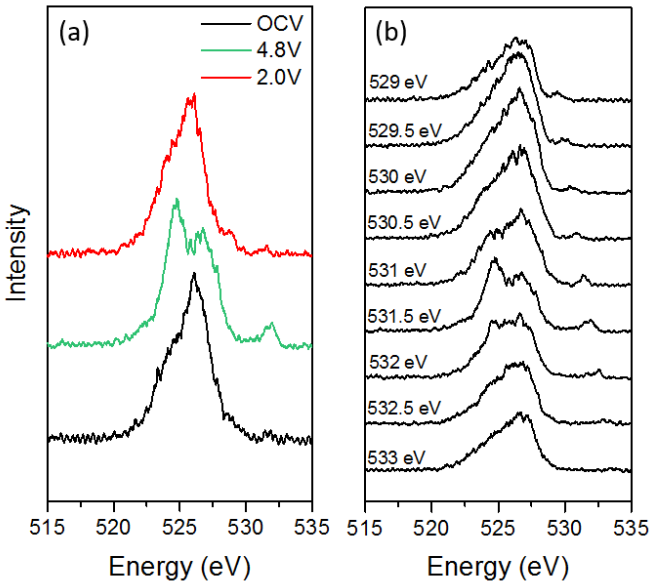

Fig. 5 (a) RIXS spectra at different states of charge collected at a RIXS energy of 531.5 eV show the appearance of a new feature at ~525 eV (b) RIXS spectra at end of charge (4.8V) collected at a range of RIXS energies show the new feature is resonant in a narrow energy range which we attribute to new, localised electronic states formed on oxygen.

Long Term Cycling Performance

Upon cycling the capacity (Fig. 3b) and voltage (Fig. S6) drop steadily at approximately the same rates of decay as seen for the Li_2VO_2F and Li_2NiO_2F. Additional cycling studies at increased C-rates reveal good retention of capacity, Fig 3b. Interestingly, from these studies it appears the fading is cycle dependent rather than time dependent as suggested by the similar rates of decay. This effect is common for all oxyfluoride materials reported so far and significant work is required to understand the source of this fading mechanism. Although this does not seem to be related to the transition metal, similar capacity losses have been observed in other all-manganese materials, such as $LiMn_2O_4$, and has been attributed to the dissolution of Mn ions into the electrolyte resulting in loss of active material from the cathode and increase in impedance of the Li metal

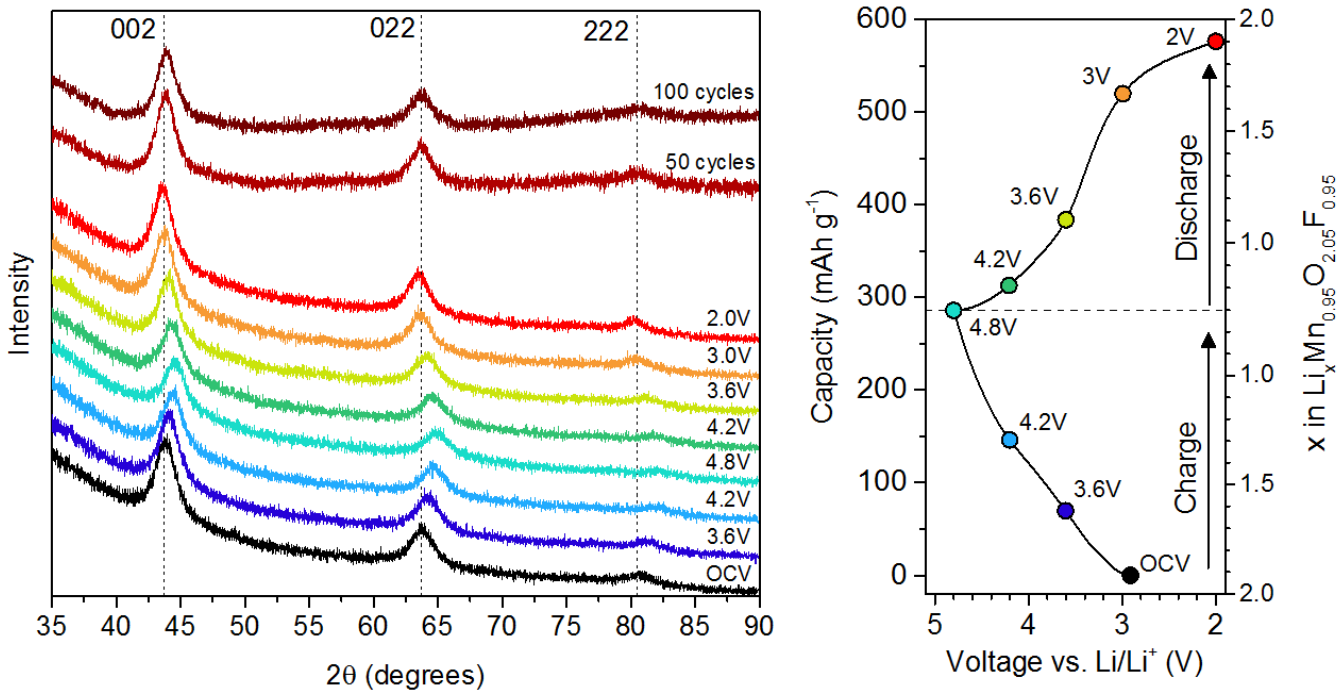

Fig. 6 Left panel: Powder X-Ray Diffraction patterns of ex situ cathode samples collected under Ar using a protective Kapton film. The two uppermost patterns correspond to cathodes cycled between 2-4.8V at a rate of C/2 (112 mA g^{-1}) and recovered after the 50th and 100th discharge to 2V. Right panel: First cycle load curve for LMOF highlighting the states of charge chosen for ex situ analysis.

anode as Mn-containing species are deposited[40–43]. To investigate Mn dissolution in LMOF, ICP-OES analysis was carried out on the residue collected from the anode, electrolyte and cell components together after long term cycling (Table S4). After 100 cycles, the percentage loss of Mn from the cathode was ~7.7% compared to a percentage capacity loss of ~53% (Fig S7) indicating that, although some Mn is lost from the cathode, it is unlikely to be the primary cause.

Another potential source of the capacity fading is gradual structural change. To study the structural evolution accompanying lithium-ion extraction and reinsertion, *ex situ* PXRD was carried out on samples at different states of charge. The results in Fig. 6 show XRD patterns recorded at progressive states of charge, which indicate a shifting of the 002, 022 and 222 peaks corresponding to a decrease and increase in lattice parameter as the structure contracts and expands isotropically with lithium content. This supports the extraction and reinsertion of lithium in the bulk of the material. The process repeats on subsequent cycling and indicates the remarkable retention of long range order even after 100 cycles. We speculate this could be due to the absence of cooperative Jahn-Teller distortion in the Rocksalt structure because of the lack of layered ordering and the disruption of centro-symmetry around Mn^{3+} centres by the presence of F^- anions.

Expansion and contraction of the electrode particles can also lead to cycle dependent capacity loss through particle disconnection over cycling and isolation of active material. However, we observed no improvement in performance after extracting a cycled electrode, re-pressing and then cycling it in a new cell, suggesting this is not the explanation as if this had been the case here we would expect some reforming of electronic contacts and a boost in capacity.

In light of our studies it is evident that further detailed work is required to understand the exact origin of the deterioration in cell performance which appears common to all oxyfluoride rock salt materials. Nevertheless, the discovery of LMOF, a promising new positive electrode material for Li-ion batteries, demonstrates for the first time that O-redox is possible in an all-manganese compound by utilising the stable disordered oxyfluoride Rocksalt structure.

Conclusions

The oxyfluoride, $Li_{1.9}Mn_{0.95}O_{2.05}F_{0.95}$, based on the stoichiometric compound Li_2MnO_2F, is the first example of an oxyfluoride exhibiting O redox. It possesses a disordered Rocksalt structure with cation vacancies. Possessing a Li:Tm ratio > 1 in the Rocksalt structure ensures enough low energy pathways for Li^+ migration. $Li_{1.9}Mn_{0.95}O_{2.05}F_{0.95}$ exhibits a high capacity to store charge of 280 mAh g^{-1} (corresponding to 960 Wh kg^{-1}) of which half, 130 mAh g^{-1}, arises from O-redox, the rest being due to $Mn^{3+/4+}$ redox. There is little evidence of any O loss from the lattice. The variation of voltage with composition is significantly more reversible than the ordered Li-rich layered compounds with overcapacity due to O-redox. This may be due to the structure already resembling that of the ordered Li-rich materials after they undergo cation disorder on cycling. An advantage of the disordered Rocksalt structured Mn

compounds is that they should avoid the cooperative Jahn-Teller distortion usually associated with Mn^{3+} in ordered structures and which often leads to poor cycling.

Conflicts of interest

There are no conflicts to declare.

Acknowledgements

The authors are grateful to EPSRC for funding this research.

Notes and references

1 J.-S. Kim, C. S. Johnson and M. M. Thackeray, *Electrochem. commun.*, 2002, **4**, 205–209.

2 Z. Lu, D. D. MacNeil and J. R. Dahn, *Electrochem. Solid State Lett.*, 2001, **4**, A191.

3 Z. Lu and J. R. Dahn, *J. Electrochem. Soc.*, 2002, **149**, A815.

4 C. S. Johnson, J.-S. Kim, C. Lefief, N. Li, J. T. Vaughey and M. M. Thackeray, *Electrochem. commun.*, 2004, **6**, 1085–1091.

5 J.-S. Kim, C. S. Johnson, J. T. Vaughey, M. M. Thackeray, S. A. Hackney, W. Yoon and C. P. Grey, *Chem. Mater.*, 2004, **16**, 1996–2006.

6 K. Luo, M. R. Roberts, R. Hao, N. Guerrini, D. M. Pickup, Y.-S. Liu, K. Edström, J. Guo, A. V. Chadwick, L. C. Duda and P. G. Bruce, *Nat. Chem.*, 2016, **8**, 684–691.

7 K. Luo, M. R. Roberts, N. Guerrini, N. Tapia-Ruiz, R. Hao, F. Massel, D. M. Pickup, S. Ramos, Y.-S. Liu, J. Guo, A. V. Chadwick, L. C. Duda and P. G. Bruce, *J. Am. Chem. Soc.*, 2016, **138**, 11211–11218.

8 N. Tran, L. Croguennec, M. Ménétrier, F. Weill, P. Biensan, C. Jordy and C. Delmas, *Chem. Mater.*, 2008, **20**, 4815–4825.

9 S. Madhavi, G. . Subba Rao, B. V. . Chowdari and S. F. . Li, *J. Power Sources*, 2001, **93**, 156–162.

10 M. Guilmard, C. Pouillerie, L. Croguennec and C. Delmas, *Solid State Ionics*, 2003, **160**, 39–50.

11 M. Sathiya, G. Rousse, K. Ramesha, C. P. Laisa, H. Vezin, M. T. Sougrati, M.-L. Doublet, D. Foix, D. Gonbeau, W. Walker, a S. Prakash, M. Ben Hassine, L. Dupont and J.-M. Tarascon, *Nat. Mater.*, 2013, **12**, 827–35.

12 M. Saubanère, E. McCalla, J.-M. Tarascon and M.-L. Doublet, *Energy Environ. Sci.*, 2016, **9**, 984–991.

13 M. Sathiya, K. Ramesha, G. Rousse, D. Foix, D. Gonbeau, A. S. Prakash, M. L. Doublet, K. Hemalatha and J.-M. Tarascon, *Chem. Mater.*, 2013, **25**, 1121–1131.

14 P. Rozier, M. Sathiya, A.-R. Paulraj, D. Foix, T. Desaunay, P.-L. Taberna, P. Simon and J.-M. Tarascon, *Electrochem. commun.*, 2015, **53**, 29–32.

15 P. E. Pearce, A. J. Perez, G. Rousse, M. Saubanère, D. Batuk, D. Foix, E. McCalla, A. M. Abakumov, G. Van Tendeloo, M.-L. Doublet and J.-M. Tarascon, *Nat. Mater.*, 2017, **16**, 580–586.

16 A. Urban, J. Lee and G. Ceder, *Adv. Energy Mater.*, 2014, **4**, 1400478.

17 J. Lee, A. Urban, X. Li, D. Su, G. Hautier and G. Ceder, *Science*, 2014, **343**, 519–22.

18 J. Lee, D.-H. Seo, M. Balasubramanian, N. Twu, X. Li and G. Ceder, *Energy Environ. Sci.*, 2015, **8**, 3255–3265.

19 N. Yabuuchi, M. Takeuchi, M. Nakayama, H. Shiiba, M. Ogawa, K. Nakayama, T. Ohta, D. Endo, T. Ozaki, T. Inamasu, K. Sato and S. Komaba, *Proc. Natl. Acad. Sci. U. S. A.*, 2015, **112**, 7650–5.

20 R. Wang, X. Li, L. Liu, J. Lee, D.-H. Seo, S.-H. Bo, A. Urban and G. Ceder, *Electrochem. commun.*, 2015, **60**, 70–73.

21 M. Nakajima and N. Yabuuchi, *Chem. Mater.*, 2017, **29**, 6927–6935.

22 N. Yabuuchi, M. Nakayama, M. Takeuchi, S. Komaba, Y. Hashimoto, T. Mukai, H. Shiiba, K. Sato, Y. Kobayashi, A. Nakao, M. Yonemura, K. Yamanaka, K. Mitsuhara and T. Ohta, *Nat. Commun.*, 2016, **7**, 13814.

23 M. Freire, O. I. Lebedev, A. Maignan, C. Jordy and V. Pralong, *J. Mater. Chem. A*, 2017, **5**, 21898.

24 M. Freire, N. V. Kosova, C. Jordy, D. Chateigner, O. I. Lebedev, A. Maignan and V. Pralong, *Nat. Mater.*, 2015, **15**, 173–177.

25 N. Dimov, A. Kitajou, H. Hori, E. Kobayashi and S. Okada, *ECS Trans.*, 2014, **58**, 87–99.

26 S.-K. Jung, H. Kim, M. G. Cho, S.-P. Cho, B. Lee, H. Kim, Y.-U. Park, J. Hong, K.-Y. Park, G. Yoon, W. M. Seong, Y. Cho, M. H. Oh, H. Kim, H. Gwon, I. Hwang, T. Hyeon, W.-S. Yoon and K. Kang, *Nat. Energy*, 2017, **2**, 16208.

27 R. Chen, S. Ren, M. Yavuz, A. A. Guda, V. Shapovalov, R. Witter, M. Fichtner and H. Hahn, *Phys. Chem. Chem. Phys.*, 2015, **17**, 17288–95.

28 S. Ren, R. Chen, E. Maawad, O. Dolotko, A. A. Guda, V. Shapovalov, D. Wang, H. Hahn and M. Fichtner, *Adv. Sci.*, 2015, **2**, 1500128.

29 R. Chen, S. Ren, M. Knapp, D. Wang, R. Witter, M. Fichtner and H. Hahn, *Adv. Energy Mater.*, 2015, **5**, 1401814.

30 Y. Tomita, H. Nasu, Y. Izumi, J. Arai, S. Otsuka, Y. Yamane, K. Yamada, Y. Kohno and K. Kobayashi, *J. Power Sources*, 2016, **329**, 406–411.

31 Y. Tomita, N. Kimura, Y. Izumi, J. Arai, Y. Kohno and K. Kobayashi, *J. Power Sources*, 2017, **354**, 34–40.

32 K. Luo, M. R. Roberts, R. Hao, N. Guerrini, E. Liberti, C. S. Allen, A. I. Kirkland and P. G. Bruce, *Nano Lett.*, 2016, **16**, 7503–7508.

33 C. P. Grey and N. Dupre, *Chem. Rev.*, 2004, **104**, 4493–4512.

34 D. R. Modeshia, R. I. Walton, M. R. Mitchell and S. E. Ashbrook, *Dalton Trans.*, 2010, **39**, 6031–6036.

35 D. Y. W. Yu, K. Yanagida, Y. Kato and H. Nakamura, *J. Electrochem. Soc.*, 2009, **156**, A417.

36 Z. Lu and J. R. Dahn, *J. Electrochem. Soc.*, 2002, **149**, A815.

37 A. R. Armstrong, M. Holzapfel, P. Novák, C. S. Johnson, S.-H. Kang, M. M. Thackeray and P. G. Bruce, *J. Am. Chem. Soc.*, 2006, **128**, 8694–8.

38 A. J. Achkar, T. Z. Regier, H. Wadati, Y.-J. Kim, H. Zhang and D. G. Hawthorn, *Phys. Rev. B*, 2011, **83**, 81106.

39 A. Léon, A. Fiedler, M. Blum, A. Benkert, F. Meyer, W. Yang, M. Bär, F. Scheiba, H. Ehrenberg, L. Weinhardt and C.

Heske, *J. Phys. Chem. C*, 2017, **121**, 5460–5466.
40 D. Jang H, Y. J. Shin and S. M. Oh, *J. Electrochem. Soc.*, 1996, **143**, 2204–2211.
41 R. J. Gummow, A. De Kock and M. M. Thackeray ', *Solid State Ionics*, 1994, **69**, 59–67.
42 G. G. Amatucci, C. N. Schmutz, A. Blyr, C. Sigala, A. S. Gozdz, D. Larcher and J. M. Tarascon, *J. Power Sources*, 1997, **69**, 11–25.
43 C. Zhan, J. Lu, A. Jeremy Kropf, T. Wu, A. N. Jansen, Y.-K. Sun, X. Qiu and K. Amine, *Nat. Commun.*, 2013, **4**, 1–8.